Journal of *Marine Science and Engineering*

MDPI

*Article*

# Experimental and Numerical Investigation of Cavity Structure Forced Water Exit from Calm Water at Constant Lifting Velocity

**Yingfei Zan [1,*], Baowen Qi [1], Song Ding [2], Ruinan Guo [1], Yong Wang [3] and Baozhong Li [4]**

[1] College of Shipbuilding Engineering, Harbin Engineering University, Harbin 150001, China
[2] China Ship Research and Development Academy, Beijing 100192, China
[3] COOEC Subsea Technology Co., Ltd., Shenzhen 518000, China
[4] China Classification Society Tianjin Branch, Tianjin 300457, China
* Correspondence: zanyingfei@hrbeu.edu.cn

**Abstract:** In marine engineering, the installation of structures inevitably involves the process of water exit. This paper studies the vertical force, the shape of the free surface, and the evolution of the water entrained in a cavity in the process of lifting a structure, so as to provide guidance for practical engineering operations. Using a 1:8 experimental model, this paper derives the governing equations based on the Reynolds-averaged Navier–Stokes approach and uses the volume of fluid method to capture the shape change of the free surface. The vertical forces obtained at different lifting speeds are found to be in good agreement with the results of previous model tests. The results show that the numerical simulation method and mesh generation described in this paper can simulate the changes in the physical quantities associated with the structure in the process of water exit. The vertical force on the structure increases nonlinearly as the lifting speed rises, and the maximum lifting speed is conservatively estimated to be 0.034 m/s using the Det Norske Veritas recommended method. The maximum vertical force occurs as the whole structure leaves the water. The water entrained in the structure is mainly located at the sides and bottom. The lifting velocity plays an important role in the water exit process. The water exit force first increases and then decreases to a stable value as the lifting velocity increases, while the maximum water exit force increases nonlinearly.

**Keywords:** water exit; model test; perforated structure; vertical force; cavity evolution



**Citation:** Zan, Y.; Qi, B.; Ding, S.; Guo, R.; Wang, Y.; Li, B. Experimental and Numerical Investigation of Cavity Structure Forced Water Exit from Calm Water at Constant Lifting Velocity. *J. Mar. Sci. Eng.* **2023**, *11*, 274. https://doi.org/10.3390/jmse11020274

Academic Editors: Simone Mancini and Momchil Terziev

Received: 13 December 2022
Revised: 19 January 2023
Accepted: 20 January 2023
Published: 25 January 2023



## 1. Introduction

With the development of engineering technology, many new items of mechanical equipment are being applied in industrial settings. This increased amount of equipment leads to an increase in energy requirements. Energy resources are unevenly distributed on land, so it is necessary to exploit offshore oil and gas. Many experts have studied the phenomena related to ocean engineering operations. Nowadays, the equipment used for marine operations is very large and complicated, which brings about higher requirements for the safety of personnel and equipment. According to the International Marine Contractors Association, of the 163 marine accidents reported in the period 2021–2022, 12.8 percent were caused by equipment failure. Thus, the analysis of the problems associated with dynamic lifting operations is of practical significance. The entry of structures into water bodies has been widely studied, but the water exit process has received far less attention. As engineering problems arise, many scenarios require a structure to exit the water during lifting operations, such as when the structure is originally placed in the incorrect position, requiring water exit and reentry, or when subsea modules require maintenance. The water exit problem thus has significant research value. The vertical forces encountered during the exit process are usually greater than those during the entry process, which means the cable strength and tension estimations are vital in ensuring operational safety. Therefore, further studies of the process of a structure exiting the water are of practical significance.

For the water exit problem, a linear model was initially used to describe the water exit problem. Nonlinear terms were introduced with the development of marine operations and the need for more accurate predictions. Korobkin et al. [1] revised a simplified model of water exit with a time-dependent radius of curvature after demonstrating the importance of nonlinear terms in forecasting hydrodynamic loads. Ma et al. [2] developed a longitudinal dynamic model for the air–water trans-media process at slow speeds and presented a novel estimation method for the fluid force. Takamure et al. [3] simulated the vertical upward launch of solid spheres through a calm water surface, helping to confirm the determination of model parameters for the water exit problem. Wang et al. [4] used methods recommended by the International Towing Tank Conference and a discretization approach based on the Courant–Friedrichs–Lewy number to analyze the numerical uncertainty of slamming loads.

The water exit process has obvious nonlinear effects, which present potential safety hazards for marine operations. Thus, many experts have applied experimental and numerical methods to study the process and its effects. Sun et al. [5] conducted experiments in which a cone-shaped axisymmetric body exited the water and recorded the cavity evolution, motion features, and dynamic loads. Zhang et al. [6] analyzed the velocity and pressure effects of water exit on an axisymmetric vehicle, with their experimental data showing that pressure fluctuations become more severe with increasing vertical exit velocity. Zan et al. [7] described an experimental study of a porous structure hovering at different positions in the splash zone, providing reference data for the installation of similar structures and validation studies. Breton et al. [8] conducted an experimental investigation of the evolution of the wetted surface and hydrodynamic force during the water exit process of axisymmetric bodies including a circular disc, cone, and sphere. Their results were in good agreement with the theoretical calculations. Zan et al. [9] studied the variations in drag force, vertical offset, and resistance during towing operations, verifying the accuracy of their numerical model. Wu et al. [10] conducted a set of experiments on the free surface deformation and dynamic changes of a rigid body exiting the water, with a particular focus on the influence of velocity and Froude number. Numerical methods typically use commercial software, open-source code computing, or the boundary-lattice Boltzmann method. Zhang et al. [11] used a two-dimensional boundary-lattice Boltzmann solver to simulate the water exit of a circular cylinder and identified the changes in the free surface and interface boundary, while Xiao et al. [12] analyzed the water exit of a circular cylinder based on the boundary-lattice Boltzmann method. Their results show that this is an effective tool for simulating water exit problems, helping to protect marine equipment from severe impact through numerical predictions. Wang et al. [13] studied the slamming impact using the Reynolds-averaged Navier–Stokes (RANS) equations and the volume of fluid (VOF) method based on OpenFOAM. Ni et al. [14] studied the water exit problem driven by a vertical dynamic force and gravity using OpenFOAM and investigated the influence of density, the structural dimensions, and initial submergence. Bhalla et al. [15] employed the fictitious domain method to simulate the water exit problem for a free-falling wedge and cylinder. Nguyen et al. [16] used the Navier–Stokes model for three-phase flows and studied the exit process of projectiles and the collapse of a cavity containing entrained water under the effect of the free surface. Moshari et al. [17] developed a finite volume discretization to determine the nonlinear free surface deformation during the water exit of a circular cylinder, while Murea et al. [18] solved a dynamic fluid-structure problem using the Navier–Stokes equations to compute the free surface force. Masaki et al. [19] performed a computational fluid dynamics (CFD) study and experimental work to examine the free decay of a platform.

Most of the research results mentioned above use experimental or numerical methods to study the water exit process of simple shapes such as cylinders or wedges. There is little prior work on the problem of structures with cavities. Zhang et al. [20] analyzed the pressure and velocity distribution during the water exit of a cylinder with a cavity and showed that the cavity collapse would cause strong pressure fluctuations. Chen et al. [21] studied the cavity shedding and collapse during the water exit of an axisymmetric

projectile, with particular emphasis on the pressure features of the water exit cavitation. Wang et al. [22] investigated the dynamic response of a structure consisting of perforated plates subjected to water impact loading.

In this paper, we describe the results from a series of experiments in which a structure with a cavity exits a body of water. Numerical simulations are carried out under the same experimental conditions. By comparing the experimental and numerical data, we verify the validity of our experimental and numerical work and derive a conservative method for estimating the maximum lifting velocity. Finally, we examine the evolution of cavity collapse and the behavior of the water entrained in the cavity.

The structure of this paper is as follows. The experimental and numerical approaches are described in Sections 2 and 3, respectively, where we introduce the experimental conditions and equipment and derive the governing equations, boundary conditions, and mesh independence. In Section 4, we discuss the validity of the experimental and numerical data and determine the maximum lifting velocity and cavity collapse effect.

## 2. Experimental Setup

### 2.1. Main Dimensions of Model

The prototype of our study model is a steel-framed structure that is used to protect the subsea pipelines running from Wenchang to Yacheng. Considering the scale of the experiment tank, the center of gravity of the model, and Froude's law of similitude, the scale ratio between the material object and the model is 8. The scale model is made of the same steel. Table 1 lists the principal dimensions. The tank size ensures that the experiments are not influenced by boundary effects.

**Table 1.** Principal dimensions of the model and tank.

| | Length (m) | Width (m) | Height (m) | Weight (Kg) |
|---|---|---|---|---|
| Entity | 17.68 | 12.1 | 3.55 | 53,248 |
| Model | 2.21 | 1.5 | 0.44 | 104 |
| Tank | 108 | 7 | 3.5 | \ |

The main body of the frame structure is made up of three rectangular parts. The large rectangular upper surface has a uniform distribution in the rectangular pool, while the perforated plate has circular perforations ($\phi = 6.25$ mm, $n = 9 \times 3 \times 2 + 12 \times 4 = 102$) in the center. The sides of the three rectangular parts are covered with skirt plates, which constitute a cavity. During lifting operations, the water flows from the pool through the perforations into the cavity, which introduces nonlinear effects to the changes in vertical force. The upper part of the rectangle is composed of intersecting groups of steel tubes welded to a single steel plate. The whole structure maintains sufficient stiffness throughout the experiment. Figure 1 shows the structure model. Figure 2 shows three sections of the structure, including two transverse sections and one longitudinal section, allowing readers to understand the cavity of the frame structure.

**Figure 1.** Model of steel framework structure.

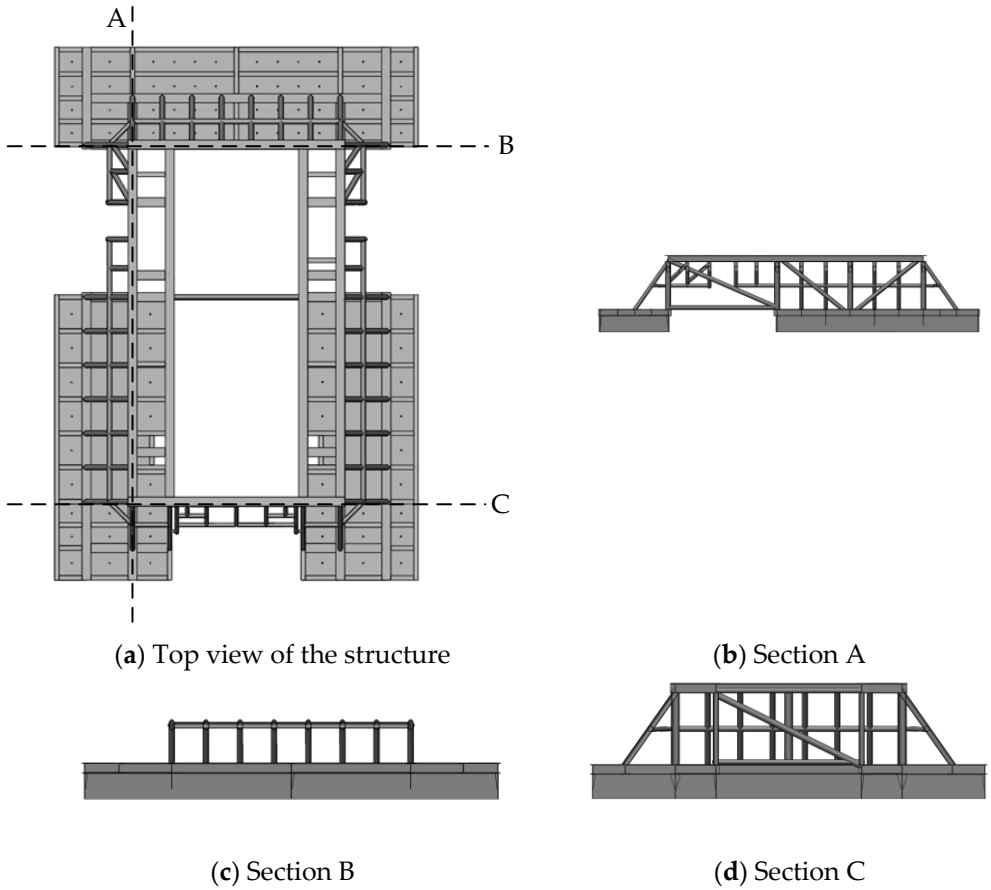


(**a**) Top view of the structure (**b**) Section A

(**c**) Section B (**d**) Section C

**Figure 2.** Sections of the structure: (**a**) section division, (**b**) longitudinal section of the left side, (**c**) transverse section of the stern, (**d**) transverse section of the stem.

### *2.2. Similarity Criterion and Hydrodynamic Coefficient*

Considering that gravity plays a major role in the lifting process and that the Froude number affects the shape of the free liquid surface, the similarity of the Froude number must be considered. The experiments conform to the principles of geometric similarity, gravitational similarity, and motion similarity according to the equality of the Froude number:

$$\frac{V_s}{\sqrt{gL_s}} = \frac{V_m}{\sqrt{gL_m}}, \tag{1}$$

where $V_s$ is the velocity of the real structure; $L_s$ is the characteristic length of the real structure; $V_m$ is the velocity of the model; $L_m$ is the characteristic length of the model; and $g$ is the acceleration of gravity.

Because only a single degree of freedom of motion is considered, the vertical force can be expressed as follows based on the Det Norske Veritas (DNV) standard [23]:

$$F_e(\mathrm{t}) = -\frac{1}{2} C_e \rho A_p v_e^2. \tag{2}$$

The dimensionless exit coefficient can then be calculated as:

$$C_e = \frac{|2F|}{\rho A_p v_e^2}, \tag{3}$$

where ρ is the density of the water; $A_p$ is the vertical projection surface area of the model (1.715 $m^2$); and $v_e$ is the vertical velocity of the model.

### 2.3. Experimental Schemes

The experiments were carried out in the towing tank at Harbin Engineering University. As shown in Figure 3, the experimental equipment was mainly composed of three parts: a forced motion mechanism, a data acquisition system, and the frame structure. The steel frame structure was placed in the center of the tank to minimize the wall effects. The top of the structure was connected to the forced motion mechanism by a welded steel plate. The lifting velocity of the mechanism was set to 0.02, 0.025, 0.03, 0.035, 0.04, 0.05, 0.08, or 0.1 m/s based on the model scale. The center of the co-rotational coordinate system (G-xyz) was located at the center of gravity, with the lengthwise direction of the model (Gx) running parallel to the long side of the tank and the downward vertical direction taken as positive.

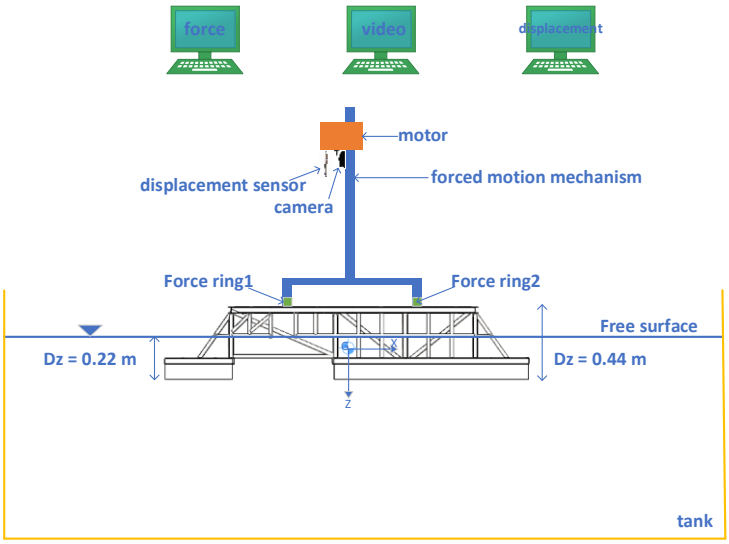


**Figure 3.** Arrangement of the experimental equipment.

Before each experiment, the model was semi-submerged at the initial stage so that the free surface was located in the middle of the upper frame, with a draft of 0.267 m. We selected this initial position because we wanted to study the vertical forces imposed by the cavity dynamics. The changes in these quantities are less significant as the upper frame exits the water, so only the cavity was submerged. Once the initial position had been set, the forced motion mechanism began to drive the model through the free surface at a constant velocity. The model then returned to the original position and the free surface was allowed to become calm before the next experiment began. During this process, the data acquisition system recorded all required data. The data acquisition system includes two force rings and a displacement sensor to measure the vertical force and velocity of the model. Two cameras (top view and side view) were used to record the motion attitude of the model and the changes in the free surface.

### 2.4. Data Analysis and Discussion

We consider the 0.1 m/s case as an example. Figure 4 shows the results of three experiments. The deviation in the maximum vertical force among the three runs is just 1.41 percent, demonstrating the reliability of the experimental data. The different times required for the free surface to become calm account for the differences in the start state in this figure, but this has no influence on the vertical force. Unless otherwise specified, all experimental data presented in this paper are the average of three runs.

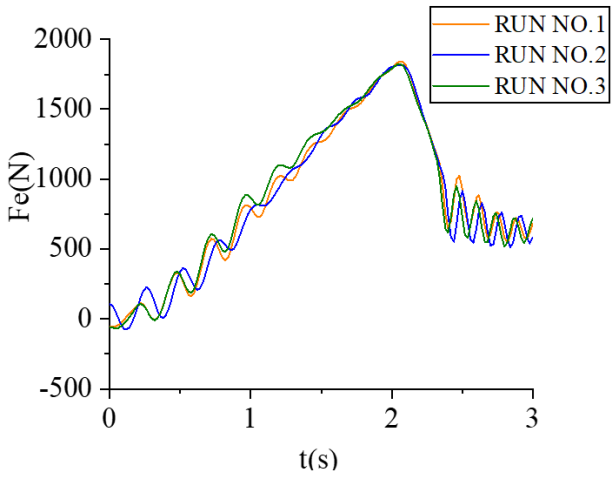


**Figure 4.** Verification of experimental results at a vertical speed of 0.1 m/s.

Figure 5 shows the time history of the experimentally determined vertical force; the time histories at different speeds exhibit the same trend. Before the structure begins to move, the vertical force and buoyancy force are in equilibrium with gravity, and the magnitude of the vertical force is very stable. The vertical force then increases almost linearly to its maximum value, at which time the structure is completely out of the water. Next, there is a decrease in the vertical force, with a small inflection point in the middle stage, before it gradually becomes steady. The increase in the vertical force depends on the lifting velocity, with the maximum vertical force occurring sooner under a higher lifting velocity. The maximum vertical force in the experimental data is 1842.5 N at a speed of 0.1 m/s and the minimum vertical force is 1558.2 N. These results are much higher than those encountered during the entry process [24].

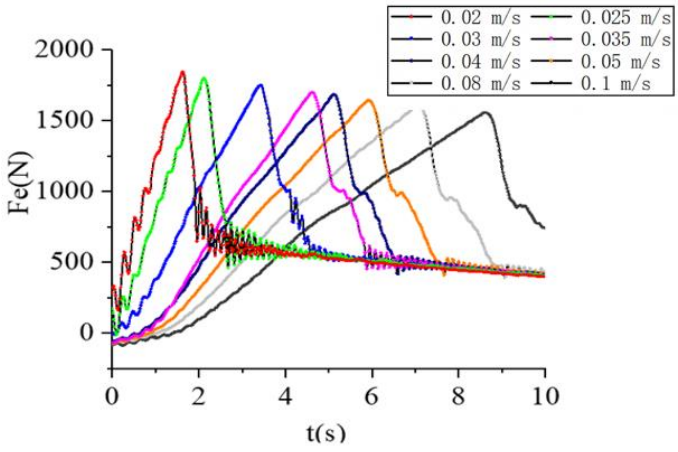


**Figure 5.** Time histories of the experimental vertical force.

To determine the relationship between the lifting velocity and the vertical force, Figure 6 presents a more intuitive picture of the changes in vertical force. As the lifting speed increases, the maximum vertical force also increases, which requires an increase in the allowable tension of the rope in the lifting operation. Therefore, the maximum lifting speed for safe operating conditions should be determined. One reliable method is discussed in Section 4.3 of this paper. Table 2 presents the maximum vertical force and growth rate based on the 0.02 m/s case (here, growth rate means the difference in the maximum water force between 0.02 m/s and other lifting speeds, divided by the maximum exit force of the 0.02 m/s case), which can be used to measure the sensitivity of this force to the lifting velocity. Figure 7 shows that the maximum vertical force increases nonlinearly with the

lifting speed, and the amplitude of the increase is larger at lower speeds. According to these limited experimental results, we can infer that the maximum force encountered in the water exit stage of the structure may have an upper limit when the velocity is sufficiently large. However, too high a velocity will introduce safety risks, so it is necessary to find a compromise that balances the safety and efficiency of lifting operations.

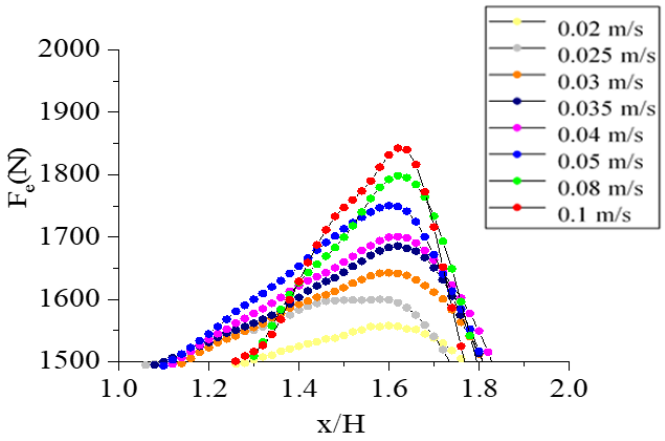


**Figure 6.** Variation in water exit force with a dimensionless coefficient of vertical height.

**Table 2.** Variation in maximum water exit force and growth rate with vertical velocity (based on 0.02 m/s case).

| **Velocity (m/s)** | **0.02** | **0.025** | **0.03** | **0.035** | **0.04** | **0.05** | **0.08** | **0.1** |
|---|---|---|---|---|---|---|---|---|
| $F_{max}$(N) | 1558.2 | 1600.1 | 1642.6 | 1685.7 | 1700.7 | 1750.3 | 1798.2 | 1842.5 |
| Growth rate | 0 | 2.67% | 5.42% | 8.18% | 9.15% | 12.33% | 15.40% | 18.25% |

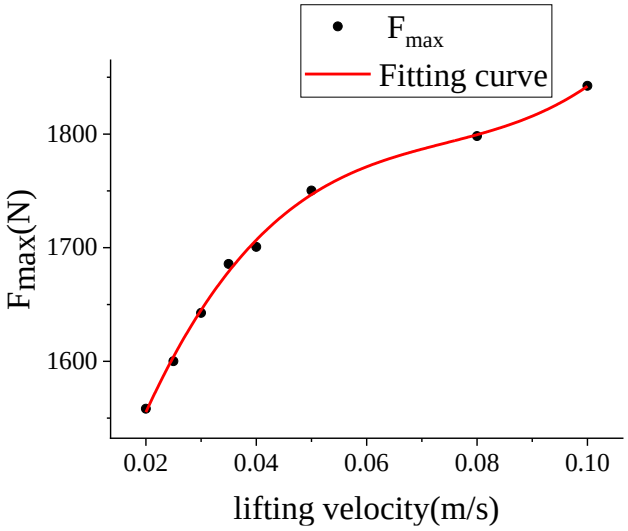


**Figure 7.** Variation in maximum water exit force with lifting velocity.

## 3. Numerical Simulations

### 3.1. Governing Equations

Using STAR-CCM+ 2020.1 [25], simulations were conducted according to the continuity equation and Reynolds turbulence equation to solve the two-phase flow model:

$$\frac{\partial \rho}{\partial t} + \nabla \cdot (\rho \overline{v}) = 0 \tag{4}$$

$$\frac{\partial}{\partial t}(\rho \overline{v}) + \nabla \cdot (\rho \overline{v} \otimes \overline{v}) = -\nabla \cdot \overline{p} I + \nabla \cdot \left(\overline{T} + T_{RANS}\right) + f_b \tag{5}$$

where $\rho$ is the density, $\overline{v}$ is the average velocity, $\overline{p}$ is the average tension, $I$ is the identity tensor, $\overline{T}$ is the average viscous stress tensor, $T_{RANS}$ is the resultant of the Reynolds stress tensor, and $f_b$ is the resultant of the volume force.

The above system of equations is not closed. The $k - \varepsilon$ turbulence model is included to complete the equation set. The finite volume method transforms the governing equations into an algebraic system; this is suitable for complex engineering problems and has good adaptability to the grid. The VOF method is used to capture changes in the free surface as the steel framework structure passes through the interface. The free surface is the interface between water and air in a gravitational field and is made up of fluid particles. The surface will become uneven when subjected to an external disturbance (e.g., wind pressure or structure motion). Gravity drives the fluid particles to their equilibrium positions, but inertia prevents this motion. The alternating motion of the fluid particles leads to changes in the free surface shape. Once the external disturbance has stopped, the viscosity of the water acts to attenuate the wave motion.

The VOF multiphase model is applied to predict the distribution of the phases and the position of the interface between the two phases in terms of the phase volume fraction with viscosity. The volume fraction of phase $i$ is defined as:

$$\alpha_i = \frac{V_i}{V}, \tag{6}$$

where $V_i$ is the volume of phase $i$ in a grid cell and $V$ is the volume of that grid cell. The sum of the volume fractions of all phases in a grid cell must be 1, i.e.,

$$\sum_{i=1}^{N} \alpha_i = 1. \tag{7}$$

The physical quantities of interface cells can be defined as:

$$\rho = \sum_i \rho_i \alpha_i, \tag{8}$$

$$\mu = \sum_i \mu_i \alpha_i, \tag{9}$$

where $\rho_i$ is the density of phase $i$ and $\mu_i$ is the dynamic viscosity of phase $i$.

### 3.2. Computational Domain and Boundary Conditions

The main frame structure is left/right symmetric, so only half of the frame is considered in the actual calculations. The whole computational domain is shown in Figure 8. The top plane of the domain is set as a pressure outlet; the posterior plane is set as a symmetry plane; the other boundaries are solid walls. An overset mesh is placed between the framework and the free surface to exchange data conveniently and obtain accurate interpolation results. The main dimensions of the computational domain are 9.08 m × 3.21 m × 5.12 m; this is sufficient for the effects of the boundaries on the flow to be regarded as negligible. The structure is initially located 0.1263 m below the free surface before being driven by the forced motion mechanism at a constant velocity through the free surface.

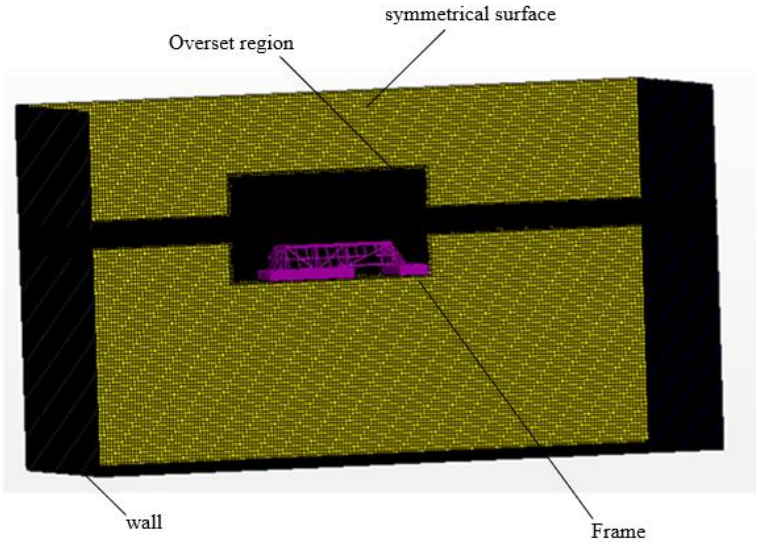


**Figure 8.** Computational domain.

### 3.3. Mesh Generation and Independence Test

The initial surface is first reconstructed to provide a high-quality volume mesh. The boundary layer is a prism layer mesh, which improves the accuracy of the solution. The whole computational domain is divided into the fluid domain, motion domain, overset domain, free surface, and frame structure. To reduce the number of cells, the basic size of the fluid domain mesh is set to 40 mm; our previous study [24] showed that this is sufficient to ensure reasonable accuracy. The motion domain, overset domain, and free surface constitute 15 percent of the basic size. This resolution ratio is sufficiently fine to allow a full exchange of momentum and energy between grid nodes and capture the deformation of the fluid particles at the free surface. The grid for the perforated layer of the frame constitutes 5 percent of the basic size. Given the diameter of the holes ($\phi = 6.25$ mm), each opening will have three grid nodes to describe its physical quantities. Thus, each scale grid has at least three layers of nodes at the boundary of the overset domain, which ensures the accurate calculation of physical quantities. Figures 9 and 10 show the mesh covering the calculation domain and the mesh describing the model.

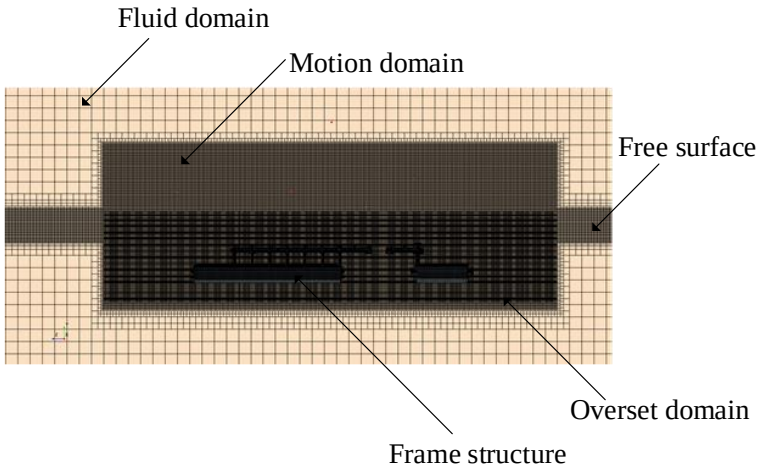


**Figure 9.** Mesh in the calculation domain.

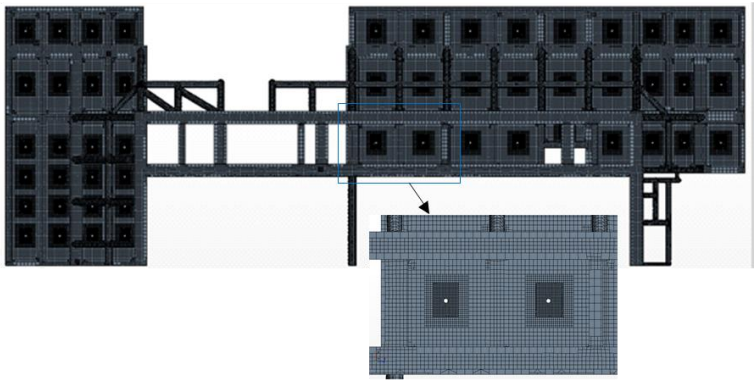

**Figure 10.** Detailed mesh of the model.

To verify the accuracy of the results and the grid independence, we considered three grid resolutions to perform the grid sensitivity study. Table 3 summarizes the settings and results for each case. We use a 0.1 m/s lifting velocity and compare the numerical results of the impulse with the three grids. We define the value of the area below the time history of the exit process as the impulse effect on the structure in the process of completely exiting from the water (Figure 11). The impulse is the integral of the exit force over the exit duration; it can assess the intensity of the exit impact. We use the impulse of the force so as to make use of all data instead of just the maximum exit force value. The relative error of impulse in each case is within 3%, which shows good agreement.

**Table 3.** Grid independence setup and impulse results.

| | Rough | Medium | Thin |
|---|---|---|---|
| Base size | 80 mm | 40 mm | 20 mm |
| Cell number | 1,215,731 | 5,066,728 | 29,261,291 |
| Impulse $(N{\cdot}s)$ | 1970.14 | 1955.26 | 1920.30 |
| GCI (%) | \ | 1.3863 | 0.7049 |

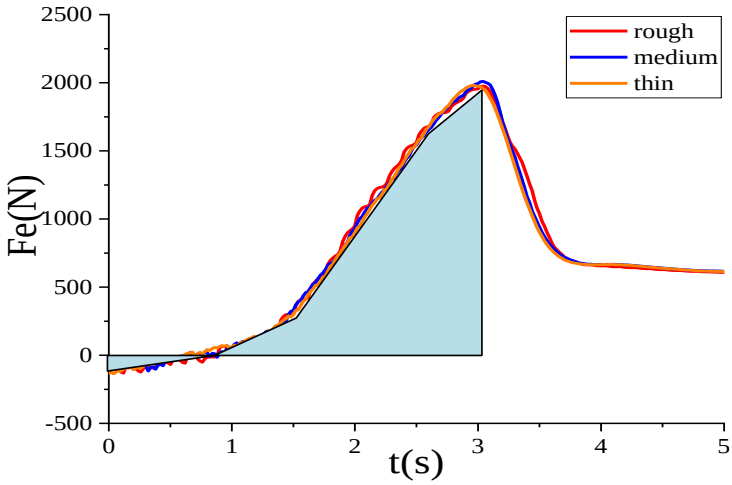


**Figure 11.** Grid independence test results at a lifting speed of 0.1 m/s.

For the CFD calculation of an engineering problem, it is necessary to assess the uncertainty error since the mesh size, which is needed to study the convergence of the results under different mesh sizes. Richardson extrapolation is used to assess the discretization error and uncertainty estimators for problems in computational fluid dynamics [26]. It needs at least three solutions; we named our numerical results as $S_1$ (solution 1), $S_2$, $S_3$.

They correspond to rough, medium, and thin mesh sizes, respectively. The results are collected in Table 3.

The rate $R$ is defined as:

$$R = \varepsilon_{21}/\varepsilon_{32} \tag{10}$$

The order of convergence $p$ can be calculated by:

$$p = ln^R/lnr \tag{11}$$

The grid convergence index (GCI) can be expressed as:

$$GCI = \frac{F_S|\varepsilon|}{r^p - 1} \tag{12}$$

where $\varepsilon_{21} = S_2 - S_1$, $\varepsilon_{32} = S_3 - S_2$, $p$ is the order of convergence, $\varepsilon$ is the relative error, $F_S$ is a safety factor, and the recommended value is 3 for two grid comparisons and 1.25 for three or more grid comparisons.

The GCI is a measure of the percentage the computed value is away from the asymptotic numerical result. It indicates an error band on how far the solution is from the asymptotic value. Based on Equations (10)–(12), the values of $GCI_{medium}$ and $GCI_{thin}$ in our study are 1.3863% and 0.7049% respectively. A small value of GCI indicates that the computation is within the asymptotic range, which means it approaches the true value. With the increasing refined grid, the computed results will not change much under this condition. The requirement of GCI [27] can be checked by the value of $GCI_{medium}/r^pGCI_{thin}$, which is approximately one and indicates that the solutions are well within the asymptotic range of convergence. Therefore, the accuracy of the numerical model grid size applied in this paper is reasonable. Considering the simulation process time and accuracy, we use the medium grid size for all subsequent simulations.

## 4. Results and Discussion

### *4.1. Validation of Experimental and Numerical Data*

The acceleration and deceleration of the experimental mechanism when starting and stopping the lifting process are ignored in the numerical simulations. We thus compare the experimental data with a fictitious numerical constant-velocity exit process. Figure 12 shows that the variation trend of vertical force is broadly consistent for the different lifting speeds. In the initial stage, the curve oscillates. During the lifting process, the vertical force on the frame remains close to zero for some time, while the frame is still in the water, as the buoyancy largely offsets the gravity. Gradually, as the framework continues to rise, the steel structure moves above the water. A linear increasing trend is then apparent, and the force quickly increases to a maximum. At the moment the steel frame is completely above the free surface, the curve exhibits an inflection point, and then drops to a stable value. We speculate that this may be because the flow through the small perforations gradually reduces the total weight of the whole structure. The maximum vertical force increases as the lifting speed rises. The maximum of 2010.3 N with a vertical speed of 0.1 m/s far exceeds the gravity of the frame itself, which is 1020.2 N. Therefore, there is some weightlessness in the steel frame during the whole process, which may have consequences for the actual lifting operation, such as cable relaxation.

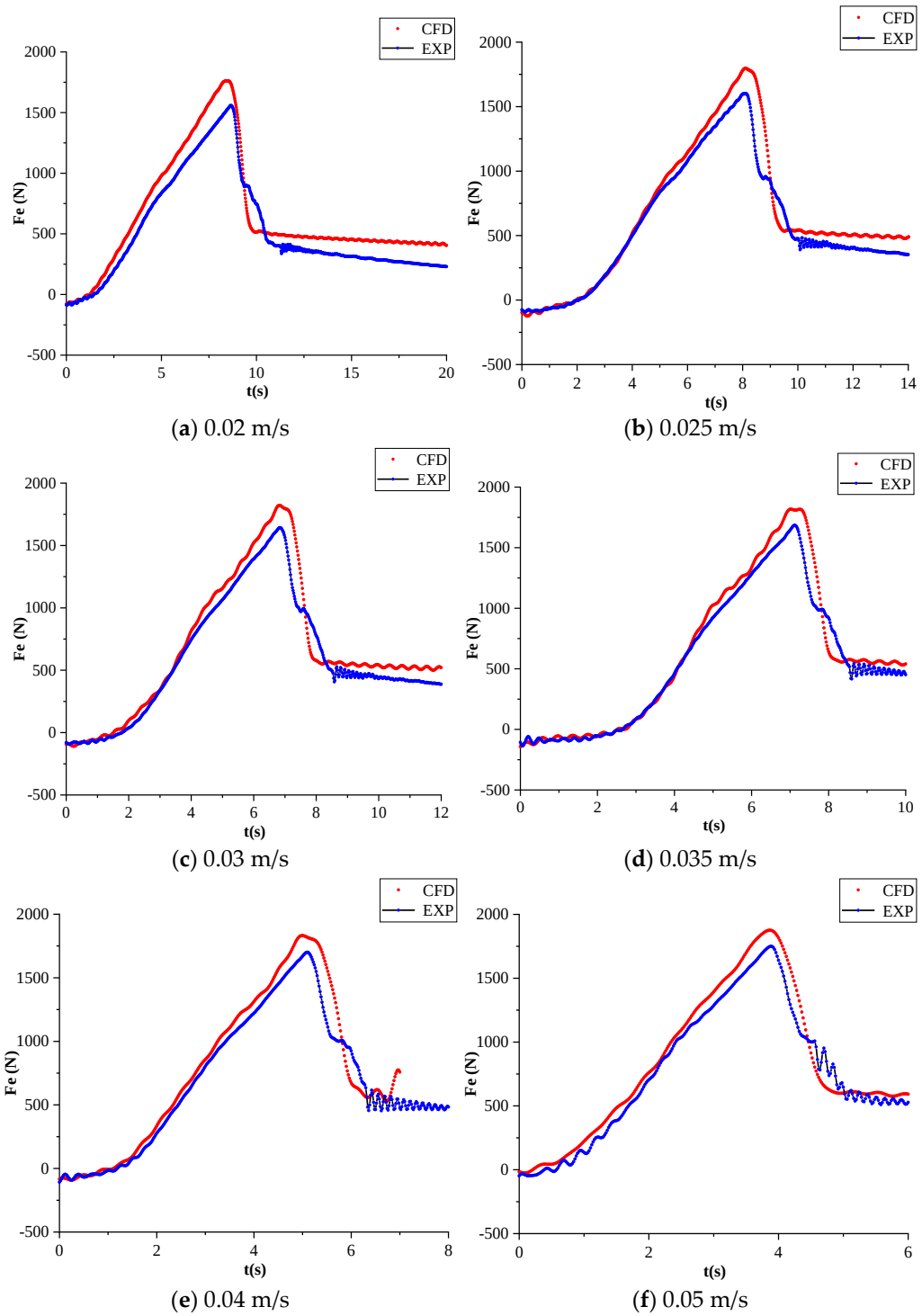


**Figure 12.** *Cont.*

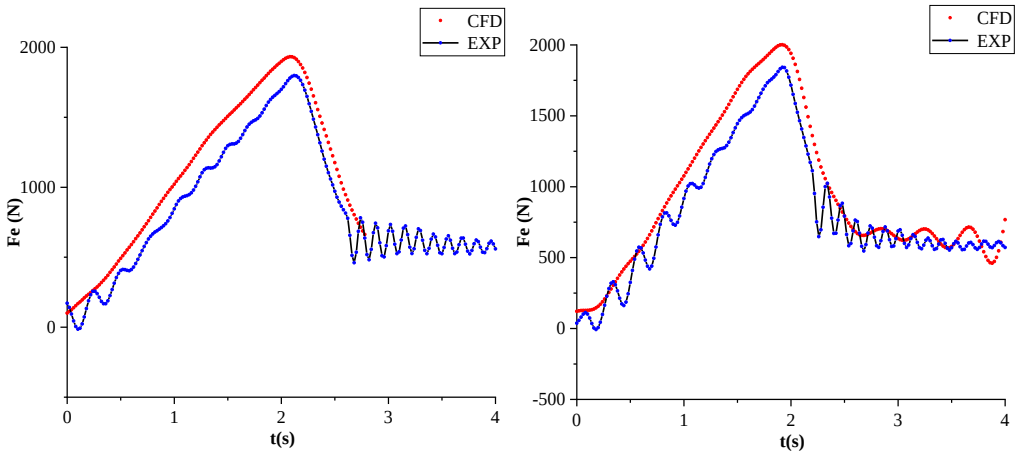


(**g**) 0.08 m/s (**h**) 0.1 m/s

**Figure 12.** Comparison of experimental and numerical vertical water exit force time history under different lifting velocities.

Data from an earlier model experiment are also shown in Figure 12. The simulation results and experimental data for the maximum vertical force are presented in Table 4.

**Table 4.** Comparison of maximum water exit force and relative error of numerical (CFD) and experimental (EXP) results.

| Velocity(m/s) | $f_{CFD}$ | $f_{EXP}$ | Relative Error |
|---|---|---|---|
| 0.02 | 1775.8 | 1558.2 | 13.96% |
| 0.025 | 1811.8 | 1600.1 | 13.23% |
| 0.03 | 1833.4 | 1642.6 | 11.62% |
| 0.035 | 1845.4 | 1685.7 | 9.47% |
| 0.04 | 1849.7 | 1700.7 | 8.76% |
| 0.05 | 1883.6 | 1750.3 | 7.62% |
| 0.08 | 1934.1 | 1798.2 | 7.56% |
| 0.1 | 2010.3 | 1842.5 | 9.11% |

The vertical force obtained from the simulations is generally larger than the experimental value. This is because the experimental steel frame continues to be impacted by water falling from the upper parts of the structure, especially when the frame has just exited the free surface completely. The whole structure suffers a severe left-lean after exiting the water completely, although this has little effect on the maximum exit force. The error in the maximum vertical force reaches 13.96% with a lifting velocity of 0.02 m/s. With an increase in lifting velocity, the error gradually decreases and stabilizes at 8%–9%, indicating that the calculation model better simulates the process of steel frame water discharge. The source of the error may be numerical when the forced motion mechanism moves at a very low speed. Both methods have large accumulated errors at low speeds, which is in good agreement with the obtained results and the actual problems that may occur.

### *4.2. Free Surface Shape and Cavity Evolution*

Figure 13 shows the four critical time nodes examined in this study. Different time nodes represent different heights of the waterplane in the water exit stage. Initially, the top of the structure is placed 0.1263 m below the calm waterplane, before being lifted at a constant velocity and touching the waterplane at $t_1$. At this stage, the model is completely submerged, its gravity is almost equal to the buoyancy, and the vertical force is relatively insignificant. At $t_2$, the cavity structure meets the interface. From $t_1$ to $t_2$, the vertical force increases as the water inside the cavity falls back into the tank. The model exits the waterplane completely at $t_3$. At this moment, the buoyancy disappears and the vertical

force reaches its maximum. We define $t_4$ as the moment when the water attached to the structure falls back into the tank. The time history of vertical force exhibits an inflection point and the gradient becomes gentler. The perforations in the frame allow the water to fall under gravity, and the vertical force decreases slowly until the model stops moving. Figure 14 shows the position of these time nodes in the vertical force time history. $t_3$ is the time of maximum vertical force, while $t_1$ and $t_4$ are inflection points prior to upward and downward trends, respectively. The vertical force time history at each lifting velocity can be used to find these time nodes. In this section, we discuss the waterplane shape of these time nodes and their effect on the vertical force. Figure 15 shows photos taken at three different time nodes.

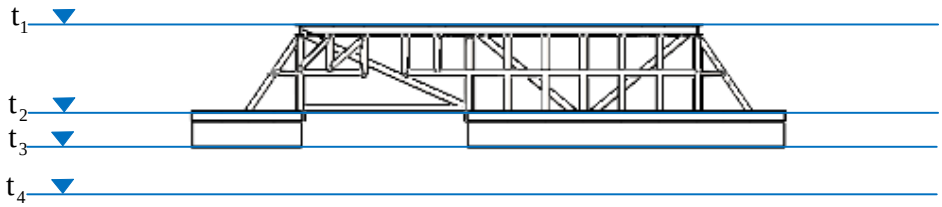


**Figure 13.** Division of the water exit stage at specific time nodes.

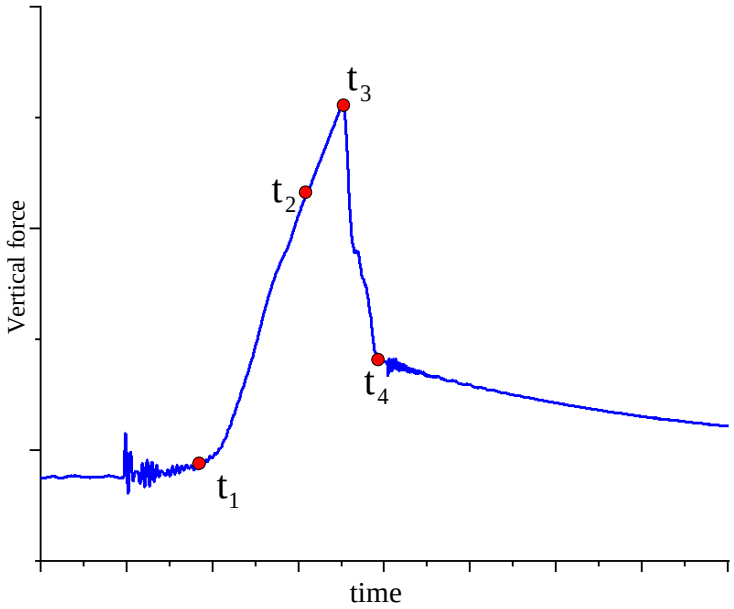


**Figure 14.** Simplified schematic figure of the time nodes in vertical force time history.

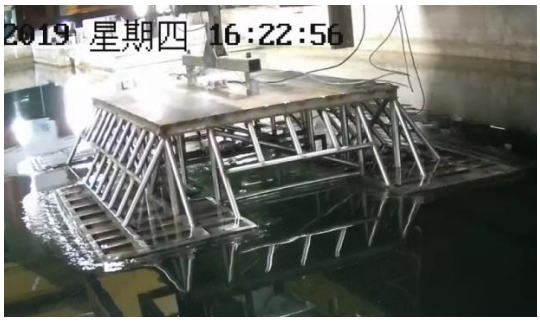


(**a**) $t = t_2$

**Figure 15.** *Cont.*


(**b**) $t = t_3$

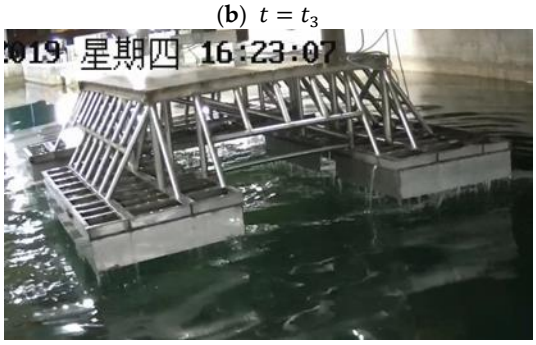


(**c**) $t = t_4$

**Figure 15.** Experimental photographs of the free surface shape under different water exit stage. The Chinese characters in the picture represent Thursday.

When the frame structure exits the water, the shape of the free surface and the pressure in the vertical plane will be influenced by the cavity [28]. We now consider these changes and discuss the relationship between shape, pressure, and velocity.

Figure 16 shows the vertical position of fluid particles at different time nodes when the lifting velocity is 0.06 m/s. The free surface shape is significantly altered by the structure and is strongly related to the shape of the structure, the lifting velocity, and the immersion depth. For convenience of description, we define the head of the parallel rectangular region as the stem and the side of the vertical parallel rectangular region as the stern. The motion of the structure drives the motion of the water near the structure, and this phenomenon obviously occurs along the side of the whole structure. The vertical position of fluid particles at the sides is always higher than that of stem or stern fluid particles; this agrees with our video of the experiment. Thus, we can conclude that green water usually occurs at the side of the structure during splash zone lifting. This provides significant guidance for the actual hoisting process of a structure.

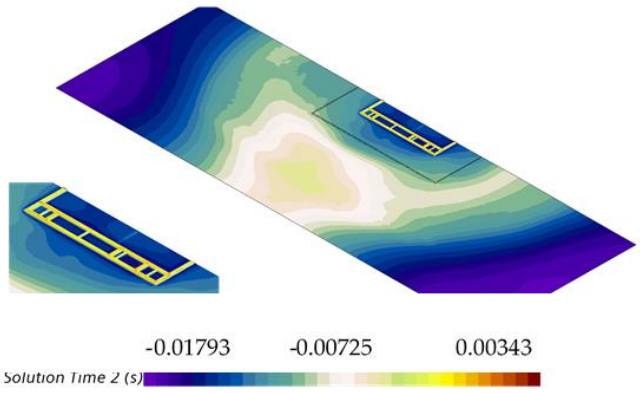


(**a**) $t = t_1$

**Figure 16.** *Cont.*

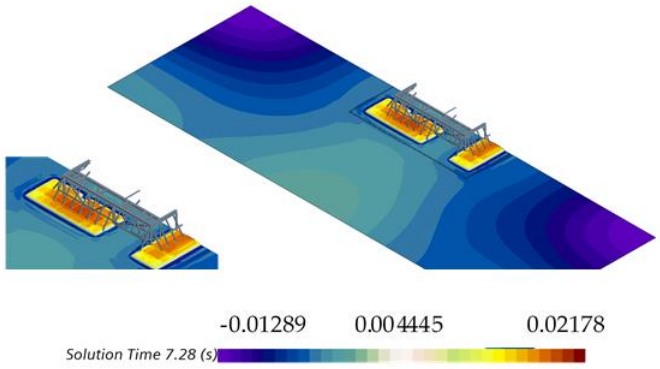


(**b**) $t = t_2$

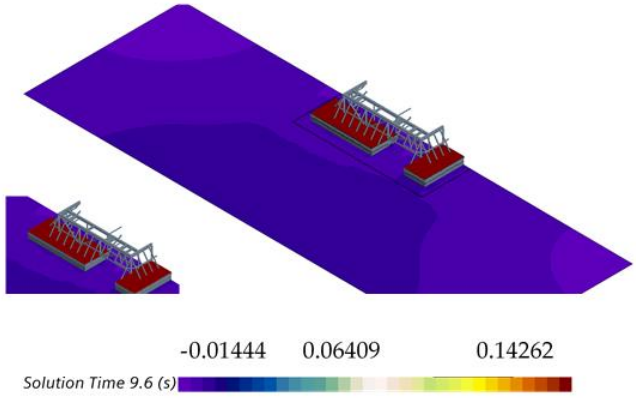


(**c**) $t = t_3$

**Figure 16.** Numerical images of the free surface shape at different time nodes with a lifting velocity of 0.06 m/s.

A vertical plane 0.52 m to the left of the center of gravity is used to monitor the overall volume change in air–water phases during the water exit stage, as shown in Figure 17. The blue parts represent air and the red parts denote water; the white lines denote the outline of the structure. All images are of the middle longitudinal section of the structure at the various exit nodes. The stem (right) represents the length of the rectangular part, while the stern (left) represents the width of the rectangular part (as shown in Figure 1). To determine the volume change mechanism, the lifting velocity is taken to be 0.04 m/s, for which the defined time nodes are marked. From $t_1$ to $t_2$, the cavity is partially submerged in the water, and the shape of the structure restrains the water inside the cavity, so the fluid particles generally remain in a rectangular shape. Once the structure exits the water completely (after $t_2$), the edges of the cavity begin to collapse, and this collapse then spreads to the bottom of the cavity. At the stem, a slender air crack cuts across the structure and water, and marginal fluid particles fall faster than the central fluid particles, producing a peak of water at the bottom of the structure. This shape continues to fall until it hits the surface. The collision causes the central fluid particles to undergo their maximum vertical deformation, whereby energy is transferred to the surrounding particles and converted into potential energy that elevates their position and washes them onto the outer surface of the structure. At the stern, the motion of the fluid particles is the same as at the stem. The collapse originates at the relatively short sides of the rectangular cavity. On the longer sides, the height of the fluid particles is uniformly distributed; this is the case for all three rectangular cavities.

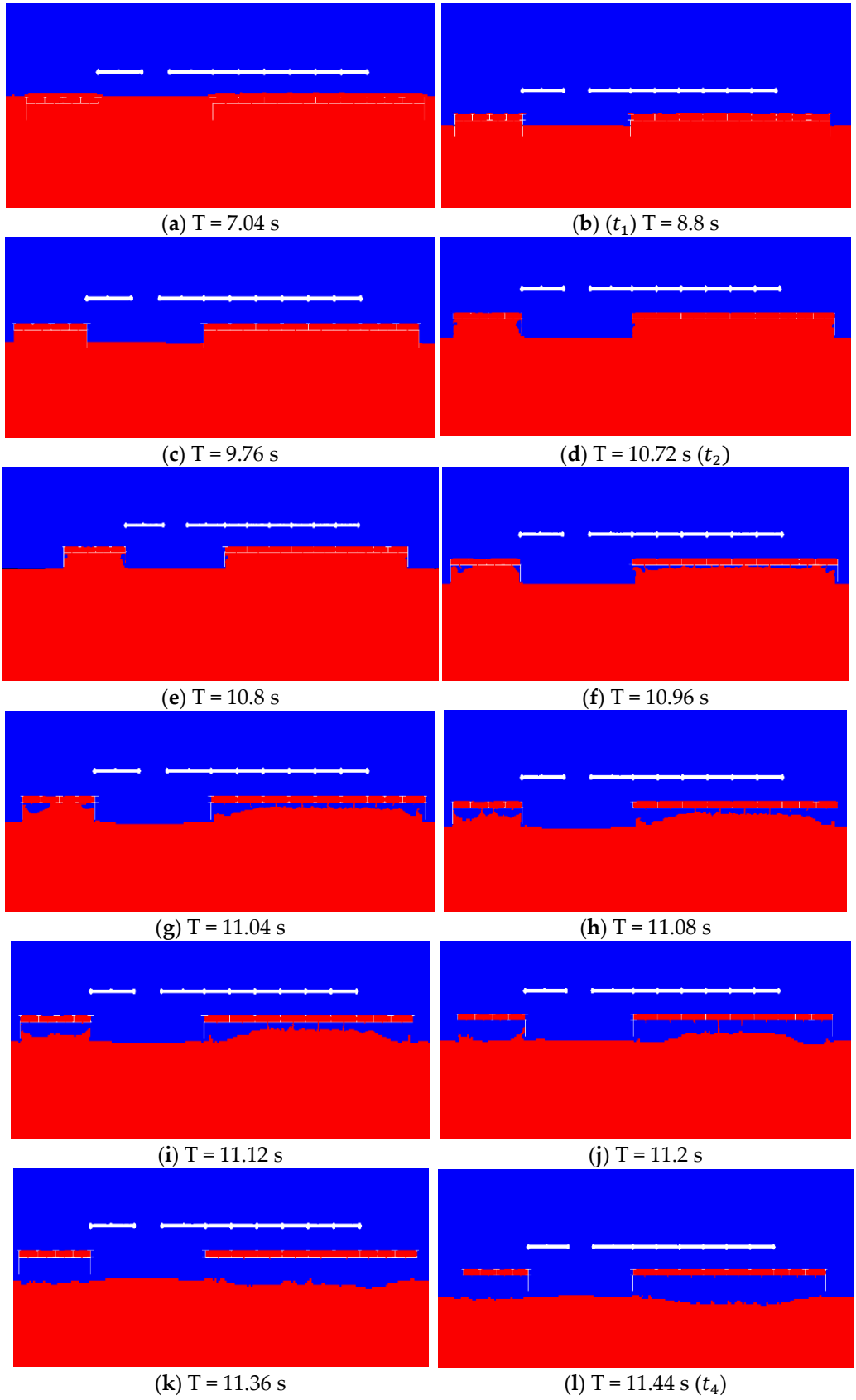


**Figure 17.** Numerical images of the volume of air and entrained water evolution.

According to this discussion, the water attached to the frame structure is mainly distributed on the side and bottom of the structure when it is discharged. Along the sides

of the structure, the height of the excited water is mainly related to the lifting speed, while the shape of the structure has a significant influence on the water column at the bottom.

### 4.3. Maximum Lifting Velocity

Based on Equation (3), the dimensionless water exit force coefficient can be expressed as:

$$C_e = \frac{|2F_{max}|}{\rho A_p v_e^2}, \tag{13}$$

where $A_p$ is the horizontal projected area minus the area of all circular perforations, which is 1.715 $m^2$ for the model considered in this study. Figure 18 shows the dimensionless coefficients of the maximum water exit force ($C_e$) at each lifting velocity. The fitting curve for $C_e$ is given by:

$$C_e = 0.70552 Fr^{-1.90396} \tag{14}$$

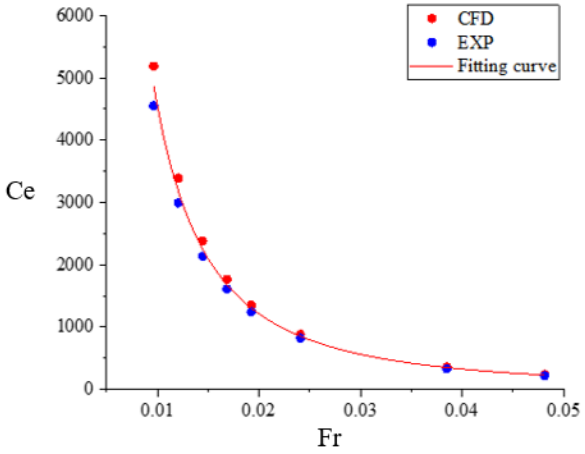


**Figure 18.** Variation in dimensionless water exit coefficient with respect to Froude number.

Through the fitting function, we have an empirical formula for estimating the Froude number of the lifting velocity under different loads. According to the DNV standards [23], the safe lifting distance during marine operations is the characteristic length of the structure plus 5 m. For the structure considered in this study, that is $2.21 \times 8 + 5 = 22.68$ m, and so the safe load corresponding to the curve is 270 t for a crane vessel with a 400 t maximum deadweight hook. The allowable safe load can be calculated as:

$$SWL_{lift} + m_{block} = (SWL_{curve} + m_{block}) \times \frac{f_{curve}}{f_{lift}} \tag{15}$$

where $SWL_{curve}$ in our case is 270 t; $m_{block}$ is the weight of the hook and cables (for the "HYSY286" vessel, this value is 8078 kg); $f_{curve}$ and $f_{lift}$ are equal to 1.15 and 1.18, respectively, according to DNV's "Modeling and Analysis of Marine Operations"; and $SWL_{lift}$ is the safe lifting load. According to similarity theory, the equation for our model and the associated structure can be expressed as:

$$\frac{v_m}{\sqrt{gL_m}} = \frac{v_e}{\sqrt{gL_e}} \tag{16}$$

Combining Equations (13)–(16), the maximum safe lifting velocity is 0.034 m/s for the object considered in this study. The above methods provide guidance for estimating the maximum safe lifting speed in offshore engineering operations.

## 5. Conclusions

In this paper, we have presented the results of model water exit experiments and conducted a series of simulations of the water exit stage of a porous structure under different lifting velocities. The experimental and numerical data are in good agreement, which lends strong empirical support to the validity and reliability of our model. In this study, we developed the process of a structure exiting the water through a simplified description, analyzed the vertical force, and compared the numerical results with experimental data. We also proposed a method of calculating the maximum lifting speed of a structure, and, finally, investigated the evolution of entrained water and the pressure distribution of the structure in the water exit stage. The conclusions from this study can be summarized as follows:

(1) The exit process of structures can be divided by time nodes according to their different characteristic contact planes. In this paper, four special time nodes were obtained, corresponding to the beginning of the water exit, the cavity contacting the water surface, the structure completely exiting the water, and the entrained water attached to the structure falling back into the water. The time history of vertical force has peak and inflection points corresponding to the selected time nodes, which provide references for describing the process of water exit.

(2) The commercial STAR-CCM+ software was used to solve the RANS equation, and the VOF method was applied to simulate the air–water interface. Several water exit simulations were carried out for structures with cavities, and the evolution of the vertical force was obtained for various lifting velocities. Compared with data from previous model tests, the maximum error of 13.96% occurred with a lifting velocity of 0.02 m/s. The minimum error of 7.56% occurred at a lifting speed of 0.08 m/s. The results show that the CFD method presented in this paper can effectively simulate the exit process of the structure and calculate the vertical water exit forces.

(3) Based on the safety of offshore hoisting operations according to DNV and similarity theory, a conservative calculation method for the maximum lifting speed of a structure was proposed. This provides a simple estimation method for actual offshore operations.

(4) The shape of the free surface and the motion of the entrained water during the exit process have been discussed. The shape of the free surface is closely related to the lifting speed and the structure shape. During the exit process, the water particles along the side of the structure are typically higher than those at the bow and stern of the structure, which means that water scouring similar to green water occurs on the sides. The water at the bottom of the rectangular cavity starts to collapse on both short sides of the rectangle, while the long sides fall to almost the average height. The distribution of attached water is symmetric with respect to the width direction of the structure, which has practical engineering significance for guiding the structure through the splash zone safely and reducing the impact of nonlinear effects.

**Author Contributions:** Conceptualization and funding acquisition, Y.Z.; methodology and writing—original draft, B.Q.; software, S.D.; investigation and writing—review, R.G.; validation, Y.W.; resources, B.L. All authors have read and agreed to the published version of the manuscript.

**Funding:** This research was funded by the Natural Science Foundation of Heilongjiang Province of China (Grant No. LH2021E048) and the High-Tech Ship Scientific Research Project of the Ministry of Industry and Information Technology of the PRC (Grant No. CBZ3N21-2).

**Institutional Review Board Statement:** Not applicable.

**Informed Consent Statement:** Not applicable.

**Data Availability Statement:** All data and models presented in this paper are available from the authors: please email us at qibaowen@hrbeu.edu.cn.

**Conflicts of Interest:** The authors declare no conflict of interest.

## References


1. Korobkin, A.A.; Khabakhpasheva, T.I.; Maki, K.J. Hydrodynamic forces in water exit problems. *J. Fluids Struct.* **2017**, *69*, 16–33. [CrossRef]
2. Ma, Z.; Hu, J.; Feng, J.; Liu, A.; Chen, G. A longitudinal air-water trans-media dynamic model for slender vehicles under low-speed condition. *Nonlinear Dyn.* **2020**, *99*, 1195–1210. [CrossRef]
3. Takamure, K.; Uchiyama, T. Effect of density of a sphere launched vertically in water on the water-surface behavior and sphere motion in air. *Phys. Fluids* **2020**, *32*, 113313. [CrossRef]
4. Wang, S.; Islam, H.; Guedes Soares, C. Uncertainty due to discretization on the ALE algorithm for predicting water slamming loads. *Mar. Struct.* **2021**, *80*, 103086. [CrossRef]
5. Sun, T.; Zhang, J.; Wei, H.; Zhang, D.; Zhang, G. Experimental investigation of the influence of floating ices constraint on the cavity dynamics of an axisymmetric body during the water exit process. *Ocean Eng.* **2022**, *244*, 110383. [CrossRef]
6. Zhang, G.; You, C.; Wei, H.; Sun, T.; Yang, B. Experimental study on the effects of brash ice on the water-exit dynamics of an underwater vehicle. *Appl. Ocean Res.* **2021**, *117*, 102948. [CrossRef]
7. Zan, Y.; Guo, R.; Yuan, L.; Ma, Q.; Zhou, A.; Wu, Z. Experimental study of a suspended subsea module at different positions in the splash zone. *Mar. Struct.* **2021**, *77*, 102935. [CrossRef]
8. Breton, T.; Tassin, A.; Jacques, N. Experimental investigation of the water entry and/or exit of axisymmetric bodies. *J. Fluid Mech.* **2020**, *901*, A37. [CrossRef]
9. Zan, Y.; Guo, R.; Yuan, L.; Wu, Z. Experimental and Numerical Model Investigations of the Underwater Towing of a Subsea Module. *J. Mar. Sci. Eng.* **2019**, *7*, 384. [CrossRef]
10. Wu, Q.G.; Ni, B.Y.; Bai, X.L.; Cui, B.; Sun, S.L. Experimental study on large deformation of free surface during water exit of a sphere. *Ocean Eng.* **2017**, *140*, 369–376. [CrossRef]
11. Zhang, G.; Yan, H.; Song, H.; Wang, H.; Hui, D. Numerical Investigation on the Deformation of the Free Interface During Water Entry and Exit of a Circular Cylinder by Using the Immersed Boundary-Multiphase Lattice Boltzmann Flux Solver. *J. Mar. Sci. Appl.* **2022**, *21*, 99–113. [CrossRef]
12. Xiao, Y.; Zhang, G.; Hui, D.; Yan, H.; Feng, S.; Wang, S. Numerical simulation for water entry and exit of rigid bodies based on the immersed boundary-lattice Boltzmann method. *J. Fluids Struct.* **2022**, *109*, 103486. [CrossRef]
13. Wang, S.; Xiang, G.; Guedes Soares, C. Assessment of three-dimensional effects on slamming load predictions using OpenFoam. *Appl. Ocean Res.* **2021**, *112*, 102646. [CrossRef]
14. Ni, B.Y.; Wu, G.X. Numerical simulation of water exit of an initially fully submerged buoyant spheroid in an axisymmetric flow. *Fluid Dyn. Res.* **2017**, *49*, 045511. [CrossRef]
15. Bhalla, A.P.S.; Nangia, N.; Dafnakis, P.; Bracco, G.; Mattiazzo, G. Simulating water-entry/exit problems using Eulerian-Lagrangian and fully-Eulerian fictitious domain methods within the open-source IBAMR library. *Appl. Ocean Res.* **2020**, *94*, 101932. [CrossRef]
16. Nguyen, V.-T.; Phan, T.-H.; Duy, T.-N.; Park, W.-G. Unsteady cavitation around submerged and water-exit projectiles under the effect of the free surface: A numerical study. *Ocean Eng.* **2022**, *263*, 112368. [CrossRef]
17. Moshari, S.; Nikseresht, A.H.; Mehryar, R. Numerical analysis of two and three dimensional buoyancy driven water-exit of a circular cylinder. *Int. J. Nav. Archit. Ocean Eng.* **2014**, *6*, 219–235. [CrossRef]
18. Yakhlef, O.; Murea, C.M. Numerical Simulation of Dynamic Fluid-Structure Interaction with Elastic Structure-Rigid Obstacle Contact. *Fluids* **2021**, *6*, 51. [CrossRef]
19. Katafuchi, M.; Suzuki, H.; Higuchi, Y.; Houtani, H.; Malta, E.B.; Goncalves, R.T. Wave Response of a Monocolumn Platform with a Skirt Using CFD and Experimental Approaches. *J. Mar. Sci. Eng.* **2022**, *10*, 1276. [CrossRef]
20. Zhang, X.-y.; Lyu, X.-j.; Fan, X.-d. Numerical Study on the Vertical Water Exit of A Cylinder with Cavity. *China Ocean Eng.* **2022**, *36*, 734–742. [CrossRef]
21. Chen, Y.; Gong, Z.X.; Li, J.; Chen, X.; Lu, C.J. Numerical Investigation on the Regime of Cavitation Shedding and Collapse During the Water-Exit of Submerged Projectile. *J. Fluids Eng. -Trans. Asme* **2020**, *142*, 011403. [CrossRef]
22. Wang, S.; Garbatov, Y.; Chen, B.; Guedes Soares, C. Dynamic structural response of perforated plates subjected to water impact load. *Eng. Struct.* **2016**, *125*, 179–190. [CrossRef]
23. DNVGL. *Modelling and Analysis of Marine Operations*; Recommended Practices DNV-RP-N103; Det Norske Veritas: Belum, Norway, 2017.
24. Zan, Y.; Guo, R.; Yuan, L.; Ma, Q.; Zhou, A.; Huang, F.; Jia, H. Experimental and numerical investigations of water entry in subsea modules with porous structures. *Appl. Ocean Res.* **2021**, *109*, 102554. [CrossRef]
25. SIEMENS. *STAR-CCM+ Users' Guide*; Version 2020.1; Siemens AG (FWB:SIE), NYSE:SI: Berlin, Gremany, 2020.
26. Phillips, T.S.; Roy, C.J. Richardson Extrapolation-Based Discretization Uncertainty Estimation for Computational Fluid Dynamics. *J. Fluids Eng. -Trans. Asme* **2014**, *136*, 121401. [CrossRef]
27. Roache, P.J. Quantification of Uncertainty in Computational Fluid Dynamics. *Annu. Rev. Fluid Mech.* **1997**, *29*, 123–160. [CrossRef]
28. Song, X.; Wu, Q.G.; Ni, B.Y.; Chen, H.L. Deformation and Bubble Entrapment of Free Surface Before Axisymmetric Bodies Detaching From Water Fully. *J. Mech.* **2019**, *35*, 863–874. [CrossRef]